Photon, scattered-atom coincidence measurements, with polarization analysis, in 3.0-keV He^+-He collisions*

F. J. Eriksen, D. H. Jaecks, W. de Rijk, and J. Macek
Behlen Laboratory of Physics, University of Nebraska–Lincoln, Lincoln, Nebraska 68588
(Received 3 February 1976)

Photon, scattered-atom coincidence measurements with polarization analysis have been made for 3.0-keV He^+-He charge-transfer collisions leading to $He(3\,^3P)$ excitation. The phase difference between the scattering amplitudes for $m_l = 0$ and $m_l = \pm 1$ magnetic-sublevel formation is an approximately constant function of scattering angle. We interpret our results using the electron promotion model and show that the phase difference should be a constant function of scattering angle and incident kinetic energy.

I. INTRODUCTION

Measurements of magnetic-sublevel populations excited in heavy-particle collisions have only recently been reported[1-4] and only for the He^+-He and He^+-H_2 collision systems. Such measurements can determine the relative importance of radial and rotational coupling within the electron promotion model, and therefore promise to be important to the development of inelastic scattering theory in atomic collisions. Two methods have been used to determine sublevel populations: (i) polarization analysis of radiation in coincidence with scattered particles, and (ii) measurement of the angular distribution of radiation, also in coincidence with scattered particles. Using the first method, de Rijk, Eriksen, and Jaecks[1] and Jaecks, Eriksen, de Rijk, and Macek[3] have made measurements of $He(3\,^3P)$ excitation in 3.0-keV He^+-He charge transfer collisions. Vassilev, Rahmat, Slevin, and Baudon[2] have measured direct excitation of He (3^3P) by 150-eV He^+ ions, and Eriksen and Jaecks[4] have seen nearly pure $He(3\,^3P)$ excitation in 1.5-keV He^+-H_2 charge transfer collisions. Using the second method Vassilev *et al.*[2] have studied the excitation of $He(3\,^1P)$ by 150-eV He^+ ions.

In this article we describe in detail measurements and calculations briefly reported earlier.[3] The polarization dependence of the coincidence rate between 3889-Å photons and scattered neutral particles has been measured as a function of incident laboratory energy T_0 and as a function of laboratory scattering angle θ. The apparatus used for the measurements is described in Sec. II and the data are presented in Sec. III. In Sec. IV we discuss our analysis of the data to determine excitation probabilities, and finally, in Sec. V we use the electron promotion model to interpret the experimental results.

II. APPARATUS

A. General vacuum system

The apparatus can be divided into two parts, (i) a source and drift region where the ion beam is produced, focused, and collimated, and (ii) a scattering region which houses the particle and photon detectors. All parts of the general vacuum system are constructed of stainless steel. The source region is pumped by a 4-in. NRC oil diffusion pump with both a freon-cooled baffle (-30 °C) and a molecular sieve trap between the diffusion pump and the vacuum system. An identical pump and baffle-trap arrangement evacuates the drift region. A Welsh 1397 forepump backs both diffusion pumps through a zeolite trap. The scattering chamber region is pumped by two NRC VHS4 4-in. oil diffusion pumps, backed by another Welsh 1397 forepump and zeolite trap. However, only molecular sieve traps separate these diffusion pumps from the vacuum system, since the pumps have very low backstreaming qualities. All four diffusion pumps can be isolated from the vacuum system by gate valves. Ion-gauge pressure measurements of the base vacuums indicate typically 2×10^{-6} Torr in the source, 1×10^{-7} Torr in the drift region, and 4×10^{-7} Torr in the scattering chamber.

B. Source and drift region

The unoplasmatron ion source and associated electrodes and lenses are constructed of stainless steel, and have been described briefly by van den Bos.[5] The ion source is separated from the magnetic field region by a cylindrical piece of glass and the source floats at a positive potential (relative to ground) which nearly determines the beam energy. Figure 1 shows a schematic diagram of the ion source giving some details not shown in Ref. 5. Two copper rods (1) support a $BaCO_3$-

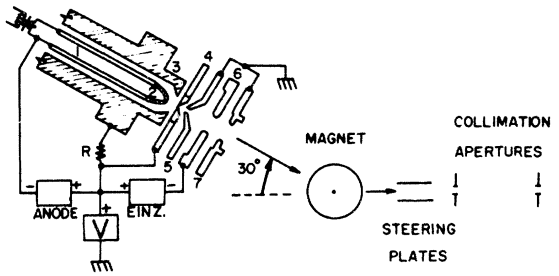

FIG. 1. Diagram of the ion source and drift region, and ion-source supply voltages.

coated platinum gauze filament (2) which is heated by an alternating current of approximately 30 A. An arc of about 1.0 A dc is struck between the anode (4) and the filament through the intermediate electrode aperture (3). Although the filament-anode bias necessary to strike the arc is about 100 V, 50–60 V typically suffice to maintain the arc. The intermediate-electrode region is filled with high-purity He gas, regulated by a leak valve to a pressure of several hundred microns as measured by a Pirani gauge. In the anode there is a copper insert with a 0.5-mm-diam aperture. Helium ions are drawn out of the arc region by the anode-to-lens (5) potential difference. Electrodes (5)–(7) form an einzel lens, (5) and (7) being grounded and (6) maintained at a positive potential with respect to ground. The He^+ beam exiting from (7) is momentum analyzed in a magnetic field and simultaneously bent through an angle of 30°. During operation the pressure near the magnetic field region is approximately 2×10^{-5} Torr.

The drift region, about 0.75 m long and constructed entirely of stainless steel, houses steering plates and the incident beam defining apertures. The apertures are slits, 0.51 mm wide each and 0.32 m apart, constructed of 0.127-mm-thick molybdenum. The second slit is actually located inside the scattering chamber, 5.08 cm from the scattering center 0. At 0 (see Fig. 2) the full width of the incident beam is 1.29 mm and it has a geometric angular spread of 0.10°.

C. Scattering chamber

The scattering chamber is a stainless-steel cylinder (about 0.40 m inside diameter and about 0.20 m inside height) with ports at various positions around the circumference. The chamber houses the interaction region, a rotatable parallel-plate electrostatic energy analyzer, and the particle detectors. The optics system protrudes down through the top of the chamber and views the scattering center from the top.

The incident beam enters the scattering chamber from the left-hand side in Fig. 2, and collides with atoms or molecules of a thermal beam near 0. The target gas beam is introduced to the scattering region by a Bendix capillary array, 9.53 mm in diameter, 1.02 mm thick, pore diameter 25 μm, and located 6.5 ± 0.5 mm from 0. The array is epoxied into a brass holder, with target gas at a pressure of several thousand microns behind the array. Under these conditions the pressure in the chamber is 4.0×10^{-5} Torr, as measured by an ion gauge. Matheson high-purity-grade gas is used for the target, its flow regulated by a Granville-Phillips leak valve. Mounted on a rotatable stainless-steel rail are two Faraday cups and a parallel-plate analyzer all made of oxygen-free copper. The Faraday cups are designed to collect the unscattered beam and thus monitor the incident-beam intensity. These cups are connected to a Keithley electrometer which typically reads an unscattered beam current of 0.5–1.0 nA. The analyzer is constructed of two copper plates 12.7 $\times7.0\times1.6$ cm^3, and has two slits, S_1 and S_2, which are continuously variable by means of a micrometer drive. The slits S_1 and S_2 are separated by 9.16 cm and are adjustable from 0.56 to 2.25 mm width, the slits being set at 2.0 mm for our measurements. A third slit S_3 is not adjustable and is 3.7 mm wide. Boron nitride insulator rods hold the plates parallel and 3.81 cm apart, and four No. 18 gauge wires serve as guard rings. The geometric angular resolution of the detector is determined by slit S_1 and the distance between the inside corners of the two Faraday cups (0.77 mm). S_1 is separated from the corners of the cups by a distance of 11.1 cm, making the geometric angular resolution of the detector 0.5°. In practice, the angular resolution is better than 0.5°, since the coincidence scattering volume is determined by the optics, incident beam, and target gas beam, as well as the detector apertures.

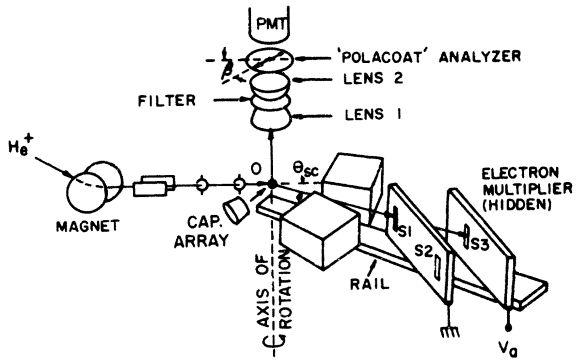

FIG. 2. Overall view of the scattering region, Faraday cups, parallel-plate analyzer, and optics system.

Behind slits S_2 and S_3 are mounted EMI 9707B electron multiplier tubes. These multipliers normally have 17 stages and are end viewing, but an extra copper beryllium dynode has been added to make them side viewing. In this experiment only the multiplier behind S_3 was in operation. The first dynode was grounded, and a bias of 4200 V was applied to the dynode chain. Pulses from the multiplier were capacitively coupled to a Johnston Laboratories PAD-1 preamplifier located outside the vacuum system. The optics system is housed in a 10-cm-o.d. stainless-steel well which protrudes down through the top of the scattering chamber and views the region near 0. The background surfaces around 0 are coated with carbon black to reduce reflections. A lens, expoxied to the bottom of the well, makes a vacuum seal between the well and the system. Both lenses used in the optics system are ultraviolet-grade quartz of focal length 63 mm and diameter 39 mm. Lens 1 is about one focal length from 0. The nearly parallel rays of light exiting from this lens pass through a 5.0-cm-diam interference filter made by Baird Atomic. The filter has a maximum transmittance of 40% at 388.6 nm and has a bandwidth of 36 Å full width at half-maximum, as specified by the manufacturer. Lens 2 focuses the remaining light to a point 2.5 cm in front of the photocathode, the light passing through a polarization analyzer before reaching the photomultiplier tube. The polarization analyzer is a quartz substrate with a special absorbing coating, the entire analyzer being manufactured by Polacoat, Inc. The coating is Polacoat 105 UV. A special property of this analyzer is its insensitivity to the entrance angle of light. The transmission axis of the analyzer makes an angle β with respect to the incident-beam direction. Photons are detected by an RCA 8850 photomultiplier tube at room temperature.

D. Coincidence electronics

Figure 3 shows a block diagram of the electronics used for determining the coincidence rate. In this experiment the uncorrelated coincidence rate is much higher than the correlated rate, and therefore it is important to make a precise determination of the uncorrelated rate. The circuit used is similar to ones previously described.[6] All amplifiers, discriminators, and AND/OR gates are manufactured by Chronetics, Inc., model Nos. 156B, 151B, and 157B, respectively.

Pulses from the photomultiplier are processed (not shown in Fig. 3), fed to a delay D, and shaped by discriminator (3). The delay D is a single long piece of RG214/U cable having low losses and small capacitance so as to minimize the degradation of the pulses. The delay D must be determined for each incident energy. Discriminator (3) shapes the pulses and routes one signal to discriminator (4) and one signal to delay D'. The signal to discriminator (4) is doubled by means of an unterminated length of RG214/U cable. Discriminator (4) shapes the doubled pulses and feeds 0.6-V 50-nsec-wide pulses to input (2) of gate I. At input (2) of gate I, the primary photon pulse is denoted by p, and the secondary pulse is denoted by s. Secondary pulses are delayed by an amount Δt, about 600 nsec, from the corresponding p pulses. The second output of discriminator (3) is delayed by an amount D', as determined by another length of RG214/U cable, and the resulting pulses are then shaped by discriminator (5) to a width of 50 nsec and fed to input (2) of gate II. The pulse at input (2) is denoted p'. The output of gate I, 100 nsec wide, is counted by a scaler N_{2A+R}, and is also fed to input (1) of gate II. The output of gate II is counted by a scaler N_A.

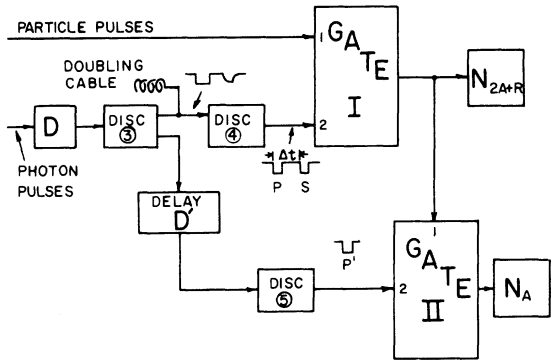

FIG. 3. Block diagram of the electronics (the main coincidence circuitry).

Real coincidences occur when a p pulse and a particle pulse (also 50 nsec wide) overlap at the input of gate I. The pulse widths and the delays D and Δt have been adjusted so that real coincidences cannot occur with secondary photon pulses s. Accidental coincidences can occur with either p or s photon pulses, however, so the output of gate I is

$$N_{2A+R} = A_p + R + A_s , \tag{1}$$

where R are real events, A_p are accidentals with p pulses, and A_s are accidentals with s pulses. The p' pulses are delayed so that at the input of gate II they overlap A_s pulses, and A_s pulses only. Thus the output of gate II is

$$N_A = A_s . \tag{2}$$

This circuit has some advantages compared to other coincidence circuitry, since it is actively

registering real events 100% of the time (as opposed to schemes which use switching methods to determine the accidental rate[7]). Also, it is superior to methods using two gates for determining R and A separately, since the present system is less susceptible to errors caused by changes in resolution of the gates.

Adjustment of delay D' was made with pulser inputs to discriminator (3) and to gate I, input (1). Pulses were fed directly to discriminator (3), and the same pulses (but delayed) were fed to gate I, input (1). The delay D was set so the pulses at gate I, input (1) were in coincidence with the s pulses at input (2). A digital delay (Berkeley Nucleonics 7030) was installed in place of D', and adjusted until the p' pulse was properly aligned with the gate-I output. The digital delay was then replaced by an appropriate length of RG214/U cable. Time measurements and alignment were made with a Hewlett Packard 1830 oscilloscope.

To adjust delay D, the digital delay was inserted in place of D and signal inputs from the photomultiplier and particle detector were connected as for a normal run. The coincidence rate of all 3889-Å photons (no polarization analysis) with neutral scattered particles was determined as a function of delay D, with results as shown in Fig. 4. The curve has about the correct width, considering the pulse widths at the input to gate I and the 112-nsec lifetime of the He($3\,^3P$) state.[8] The delay which gave a maximum in this curve was chosen for delay D, and a single length of RG214/U was cut to replace the 7030 digital delay.

The electronics were periodically checked by inserting an improper delay in place of D and verifying that normal signal inputs produced zero real coincidences.

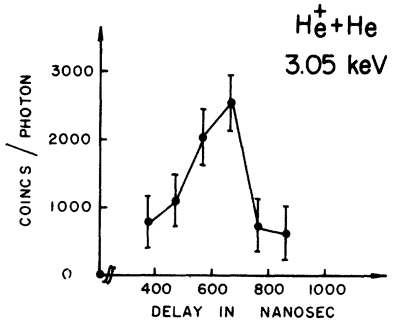

FIG. 4. The number of real coincidences divided by the number of photon counts vs the delay D (see Fig. 3). Data shown represent coincidences between 3889-Å photons with no polarization analysis and scattered particles of any charge state. Data are for 3.05 keV incident energy and 1.0° scattering angle.

III. DATA

Measurements of the total charge transfer probability P_{ex} were made as a function of scattering angle θ and are shown in Fig. 5. The measurements were made using the neutral particle detector behind $S3$, counting the number of particles reaching this detector with and without voltage applied to the analyzer. The maxima and minima agree in angular position ($\pm 0.1°$) with the data of Nagy *et al.*[9] There is a damping of both maxima and minima due to our large angular resolution, and a slight downward shift of P_{ex} presumably due to a difference in the efficiencies for neutral and ion detection. If α' denotes the efficiency, we estimate that $\alpha'_{neu}/\alpha'_{ion} \simeq 0.8$.

Measurements of the scattered neutral signal indicate a linear pressure dependence at a scattering chamber pressure of 4×10^{-5} Torr. This pressure was measured with an ionization gauge and 4×10^{-5} Torr is the chamber pressure during a run. As a further check for any pressure-dependent effects, coincidence data at 3.05 keV, 1.60° were obtained at chamber pressures of 2×10^{-5} and 4×10^{-5} Torr, there being no important differences in our calculated parameters.

Incident beam profiles were taken to locate beam zero, which remains constant to within 0.1° over a 1.5-yr period.

Figure 6 shows the coincidence rate between all 3889-Å photons (no polarization analysis) and all scattered particles (neutrals and ions), as a function of angle θ. These data confirm that the threshold for the excitation of the He($3\,^3P$) state occurs at values smaller than 3 keV deg, already indicated by the work of Barat *et al.*[10] Barat *et al.* reported the direct excitation cross sections for states $n \geq 3$ in $He^+ + He$ collisions, there being a peak in this cross section near 1.3 keV deg.

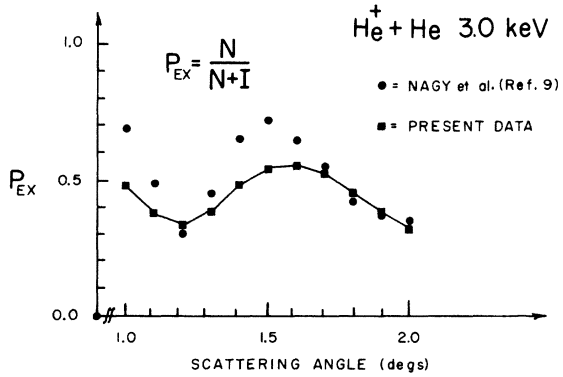

FIG. 5. The charge exchange probability P_{ex} vs scattering angle θ (in deg) at 3.0 keV. Comparison of present results with the data of Nagy *et al.* (Ref. 9).

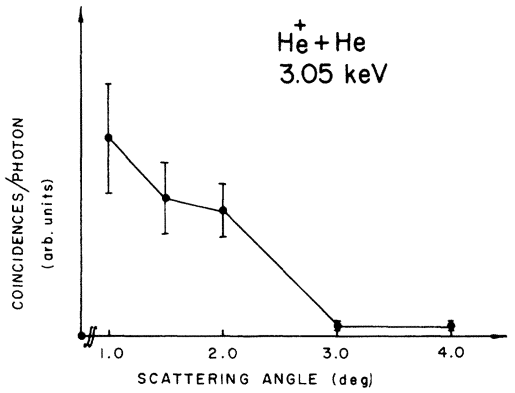

FIG. 6. The number of coincidences (between all 3889-Å photons and all scattered particles) per scattered photon vs scattering angle θ.

As shown in Fig. 7, measurements were also made of the noncoincidence polarization, that is, the polarization of all 3889-Å radiation regardless of the scattering angle of the particles. The data show slightly more polarization parallel to the incident beam than perpendicular. Although there are no data available for comparison, the polarization fraction is in fair agreement with the measurements of de Heer *et al.*[11] at higher energies

For our coincidence measurements, a typical data set for each run included laboratory energy T_0, the laboratory scattering angle θ, the polarizer angle β, the pressure in the scattering chamber, the beginning and ending time, the number of photons and particles detected, and the readings on the scalers from gate I, denoted N_{2A+R} and from gate II, denoted N_A. The number of real events R'_M is determined by doubling N_A and subtracting it from N_{2A+R}. The quantity R_M is R'_M divided by the number scattered neutral particles times 10^{-9}.

The error in the measured number R'_M is given by the square root of N_{2A+R}, as the following analysis indicates. The parameter R'_M is

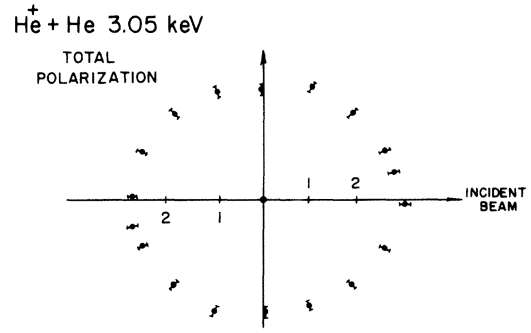

FIG. 7. Photon count rate in counts per sec vs polarizer angle β, noncoincidence, at 3.05 keV.

$$R'_M = N_{2A+R} - 2N_A = (A_p + R + A_s) - 2A_s$$
$$= A_p - A_s + R, \tag{3}$$

where A_p, A_s, and R are defined in Sec. II D and are independent variables. The estimated standard deviation in R'_M is therefore

$$\sigma^2_{R'_M} = \sigma^2_{A_p} + \sigma^2_{A_s} + \sigma^2_R = A_p + A_s + R,$$
$$\sigma_{R'_M} = (A_p + A_s + R)^{1/2} = (N_{2A+R})^{1/2}, \tag{4}$$

where the errors have been assumed to combine quadratically and the standard deviations in A_p, A_s, and R are $\sqrt{A_p}$, $\sqrt{A_s}$, and $\sqrt{R}$.[12] The error σ_{R_M} is $\sigma_{R'_M}$ divided by the number of scattered neutral particles times 10^{-9}.

Runs are usually 24 h long, and are made at four polarizer angles (0°, 45°, 90°, 135°) for each scattering angle θ. At least two runs are made at each polarizer angle β; the average value R_{av} and the estimated standard deviation $\sigma_{R_{av}}$ are determined from

$$R_{av}(\beta) = N^{-1} \sum_{i=1}^{i=N} R_M^{(i)}(\beta),$$
$$(\sigma_{R_{av}})^{-2} = \sum_{i=1}^{i=N} (\sigma_{R_M^{(i)}})^{-2}, \tag{5}$$

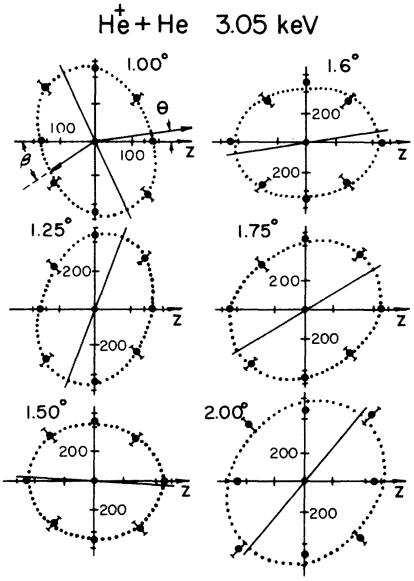

FIG. 8. Polar plots of $R_{av}(\beta)$ vs β for six scattering angles θ at 3.05 keV. The large solid dots with error bars are data, and the smaller dots without error bars are least-squares best fits of the data to Eq. (8). The major axes of the best fits are shown by solid lines. The numbers on the axes represent the scale of R_{av} in real coincidences per 10^9 scattered neutrals. For each polar plot, the incident beam direction coincides with the z axis and neutral particles are detected at an angle θ above the z axis.

where N is the number of runs at a given β and θ. Figure 8 shows the average values $R_{av}(\beta)$ at 3.05 keV for 1.00°, 1.25°, 1.50°, 1.60°, 1.75°, and 2.00°. Data not shown in Fig. 8, but taken at 1.00°, 3.05 keV for $\beta = 22.5°$ and 112.5°, confirm the hourglass shape of the patterns. Typically, a polarization pattern requires 2 weeks of running time. The dotted lines are computer fits to the data, as described in the next Sec. IV.

In all polarization patterns, the He^+ beam direction is identical with the z axis, and the scattered neutral beam is detected above the positive z axis. The most apparent feature of these patterns is their rotation as a function of scattering angle.

IV. ANALYSIS OF DATA

The polarization patterns have been analyzed using the results of Macek and Jaecks,[13] who derive a general expression for the coincidence rate in an atomic scattering process. We have evaluated this expression for the particular case of $He(3^3P)$ excitation in He^+-He charge transfer collisions, where the excited $He(3^3P)$ atom decays to the $He(2^3S)$ state. We obtain

$$I(\beta) = C[28\sigma_0 + 26\sigma_1 + 15(2\sigma_0\sigma_1)^{1/2}\cos\Delta\phi\,\sin 2\beta + (30\sigma_1 - 15\sigma_0)\sin^2\beta], \quad (6)$$

where $I(\beta)$ is the coincidence rate between scattered particles and photons emitted at 90° with respect to the collision plane, C is an unknown constant depending, for example, on detector efficiencies, σ_0 and σ_1 are the differential cross sections for exciting the $m_l = 0$ and $m_l = \pm 1$ magnetic substates of $He(3^3P)$, $\Delta\phi$ is the phase angle between the scattering amplitudes (a_0 and a_1) for $m_l = 0$ and $m_l = \pm 1$ excitation, and β is the angle of the polarization analyzer (see Fig. 2). Equation (6) is generally hourglass shaped on a polar plot of $I(\beta)$ vs β. The quantity $R(\beta)$ we report in Fig. 8 is related to $I(\beta)$ as follows:

$$R(\beta) = I(\beta)/I_N = I(\beta)/(K'\sigma_N), \quad (7)$$

where $R(\beta)$ is the number of coincidences per 10^9 scattered neutral particles, I_N is the rate of neutral scattered particles times 10^{-9}, σ_N is the differential cross section for the scattering of a neutral particle to angle θ, and K' is an unknown constant. In terms of P_0 and P_1, $R(\beta)$ is

$$R(\beta) = [28P_0 + 26P_1 + 15(2P_0P_1)^{1/2}\cos\Delta\phi\,\sin 2\beta + (30P_1 - 15P_0)\sin^2\beta], \quad (8)$$

where

$$P_0 = K\sigma_0/\sigma_N, \quad P_1 = K\sigma_1/\sigma_N. \quad (9)$$

From a computer least-squares best fit of our data by Eq. (8) we determine the quantities P_0, P_1, and $\Delta\phi$ as a function of angle β. The quantities P_0 and P_1 have units of coincidences per 10^9 scattered neutral particles, and are proportional to the probabilities σ_0/σ_N and σ_1/σ_N. The best fit was obtained by minimizing the weighted mean-square deviation $\bar{\Delta}$, i.e.,

$$\bar{\Delta} = \sum_{\beta=0°,45°,90°,135°} [R(\beta) - R_{av}(\beta)]^2(2\sigma^2_{R_{av}})^{-1}, \quad (10)$$

where $R(\beta)$ is given by Eq. (8), and $R_{av}(\beta)$ and $\sigma_{R_{av}}$ are the measured average coincidences per 10^9 scattered neutrals and the standard deviation of R_{av}. In practice, the parameters varied in the minimization were R_{max}, R_{min}, and ϑ, where R_{max} and R_{min} are the values of $R(\beta)$ along the major and minor axes of the hourglass, and ϑ is the angle of the minor axis with respect to the incident direction.

For all polarization patters, only one minimum in $\bar{\Delta}(R_{max}, R_{min}, \vartheta)$ was found. The program took the best values of R_{max}, R_{min}, and ϑ and calculated the values of P_0, P_1, and $\Delta\phi$ according to the relations

$$\begin{aligned} P_0 &= [R_{max} + R_{min} - (R_{max} - R_{min})\cos 2\vartheta](82)^{-1} \\ &\quad - [(R_{max} - R_{min})\cos 2\vartheta]\tfrac{13}{615}, \\ P_1 &= [R_{max} + R_{min} - (R_{max} - R_{min})\cos 2\vartheta](164)^{-1} \\ &\quad + [(R_{max} - R_{min})\cos 2\vartheta]\tfrac{14}{615}, \\ \cos\Delta\phi &= -(R_{max} - R_{min})(\cos 2\vartheta)/(450P_0P_1)^{1/2}. \end{aligned} \quad (11)$$

Errors in R_{max}, R_{min}, and ϑ were estimated from values of $\bar{\Delta}$ according to the relation[12]

$$(\sigma_\xi)^{-2} = \frac{\partial^2\bar{\Delta}(\xi)}{\partial\xi^2} \cong \frac{\bar{\Delta}(\xi_{i+1}) - 2\bar{\Delta}(\xi_i) + \bar{\Delta}(\xi_{i-1})}{\Delta\xi}, \quad (12)$$

where the parameter ξ stands for either R_{max}, R_{min} or ϑ, σ_ξ is the estimated standard deviation in the parameter ξ, $\Delta\xi = \xi_{i+1} - \xi_i = \xi_i - \xi_{i-1}$, and ξ_i gives the minimum $\bar{\Delta}$. From the errors in R_{max}, R_{min}, and ϑ, Eqs. (11) were used to determine the errors in P_0, P_1, and $\Delta\phi$ according to[12]

$$\sigma^2_{P_0} = \sum_\xi \frac{\partial^2 P_0}{\partial\xi^2}\sigma^2_\xi, \quad (13)$$

etc., where ξ again stands for R_{max}, R_{min}, or ϑ.

For comparison of theory with experiment, more relevant quantities are σ_0/σ_T and σ_0/σ_T, where σ_T is the cross section for scattering of all particles (regardless of charge state) to an angle θ. To convert from P_0 and P_1 we note that

$$\sigma_T = \sigma_N/P_{ex}, \quad (14)$$

where P_{ex} is the total charge transfer probability.

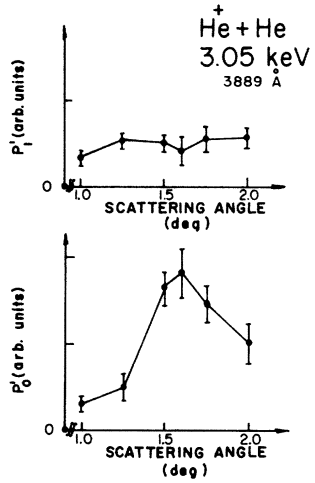

FIG. 9. Probabilities P_0' and P_1' for exciting the $m_l=0$ and $m_l=\pm1$ states as a function of lab scattering angle θ. P_0' and P_1' are the number of coincidences per 10^9 scattered particles (neutral or charged).

Then from the definitions of P_0 and P_1

$$P_0 = K\sigma_0/\sigma_N = (K\sigma_0/\sigma_T)(P_{ex})^{-1},$$
$$P_1 = K\sigma_1/\sigma_N = (K\sigma_1/\sigma_T)(P_{ex})^{-1}. \tag{15}$$

Therefore we define P_0' and P_1' as

$$P_0' \equiv K\sigma_0/\sigma_T = P_{ex}P_0,$$
$$P_1' \equiv K\sigma_0/\sigma_T = P_{ex}P_1. \tag{16}$$

We have used our own measured values of P_{ex}, shown in Fig. 6, to convert P_0 and P_1 to P_0' and P_1' according to Eqs. (16). The parameters P_0', P_1', and $\Delta\phi$ are plotted versus scattering angle θ in Figs. 9 and 10.

The values of P_0' and P_1' show that the excitation of the $m_l=\pm1$ states is rather constant as a function of angle, whereas the excitation of the $m_l=0$ state has a large peak near 1.6°. The most important feature of the data, however, is the nearly constant 90° value of the phase difference $\Delta\phi$.

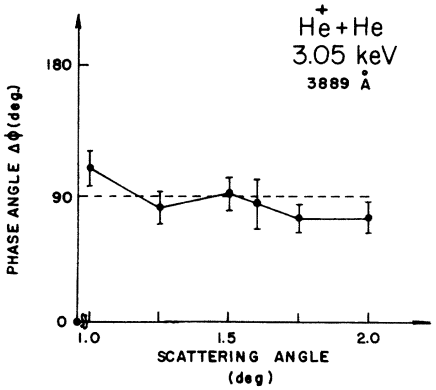

FIG. 10. Phase angle $\Delta\phi$ vs scattering angle. Since only linear polarization analysis was made, $\Delta\phi$ is undetermined to within a sign.

V. THEORY

We interpret these data using the electron promotion model, assuming a Landau-Zener crossing between the $1s\sigma_g(2p\sigma_u)^2A\,^2\Sigma_g$ and $(1s\sigma_g)^2 4d\sigma_g\,^2\Sigma_g$ He_2^+ electronic energy curves. A correlation diagram for the He_2^+ system is shown in Fig. 11. Bardsley[14] has calculated the molecular energies of some of the states leading to $1s2p$ excitation of He, these states crossing the $1s\sigma_g(2p\sigma_u)^2A\,^2\Sigma_g$ state near 1.5 a.u. The crossing of the $A^2\Sigma_g$ state and the $(1s\sigma_g)^2 4d\sigma_g$ state is therefore expected to occur at an internuclear distance of less than 1.5 a.u., i.e., 1.2–1.4 a.u. The exact position of the crossing, however, is unimportant for our analysis.

There are alternate ways of exciting the $He(1s3p)$ state. As shown in Fig. 11, it is possible for the incident $A^2\Sigma_g$ state to excite the $(1s\sigma_g)(2p\sigma_u)(2p\pi_u)^2\Pi_g$ state by rotational coupling at small R. Barat *et al.*[10] explain excitation of $n=2$ states of He in He^+-He collisions on the basis of this crossing. In order to excite the $1s3p$ state of He, the $^2\Pi_g$ must couple at large R with states which dissociate to $1s3p$ of He, and it is expected that such coupling is small. Also, it is possible to excite the $1s\sigma_g(2p\pi_u)^2\,^2\Delta_g$ state at small R and again have couplings at large R which mix the $^2\Delta_g$ state with states that lead to $1s3p$. The importance of these other mechanisms has not yet been established.

Consider the $1s\sigma_g(2p\sigma_u)^2A\,^2\Sigma_g$ to $(1s\sigma_g)^2 4d\sigma_g\,^2\Sigma_g$ mechanism, and assume that the scattered particle follows a nearly-straight-line trajectory, as shown in Fig. 12. The value of the crossing radius

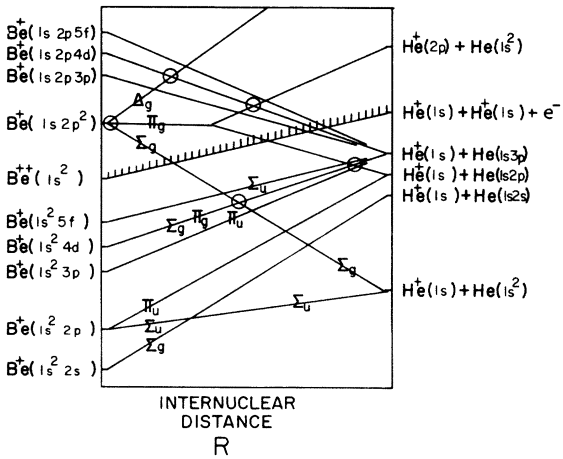

FIG. 11. A correlation diagram of diabatic states constructed following Barat *et al.* (Ref. 10) and Barat and Lichten (Ref. 16).

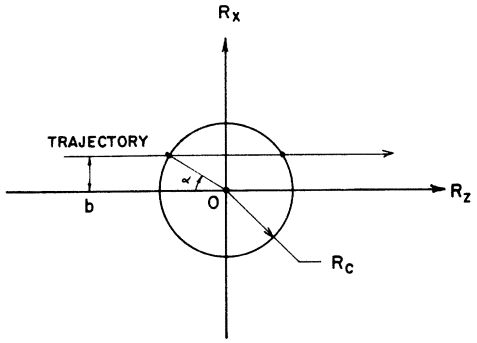

FIG. 12. A schematic diagram of the internuclear vector $\vec{R}$ during the collision, assuming a straight-line trajectory. R_c is the internuclear distance at which the excitation $1s\sigma_g(2p\sigma_u)^2$ to $(1s\sigma_g)^2 4d\sigma_g$ is presumed to occur, and b is the impact parameter.

R_c will be about 1.3 a.u. Compared to the size of the $4d\sigma_g$ wave function (the first radial node of a hydrogenlike $4d$ wave function occurs at about 6 a.u. for $Z=2$), R_c is small. Therefore the molecular energies of the $4d\sigma_g$ and $4d\pi_g$ states will be nearly degenerate. In fact, the energy separations can be estimated for the H_2^+ levels. The H_2^+ $4d\sigma_g$ and $4d\pi_g$ levels are separated[15] by approximately $\Delta E = 0.01$ a.u. at $R = 2$ a.u. This energy is to be compared with the angular frequency of the rotating internuclear axis. For an internuclear velocity of 0.1 a.u. corresponding to an incident He^+ energy of 1 keV, and an impact parameter $b = 1$ a.u., the angular frequency is of the order of 0.1 a.u. This is large compared to ΔE; consequently, the assumption that $\Delta E = 0$ is acceptable even for incident energies of the order of a few hundred eV. On the incoming passage of the crossing, the $4d\sigma_g$ level is populated when the internuclear axis is oriented at an angle α, such that

$$\sin\alpha = b/R_c \tag{17}$$

where b is the impact parameter. Subsequent motion of the nuclei is accompanied only by a phase change of the wave function, since in the approximation that the $4d\sigma_g$ and $4d\pi_g$ states are degenerate, the charge distribution maintains the orientation it had at the time of the level crossing. A similar transition takes place on the outgoing passage of the crossing.

We have taken the point of view that the excited wave function stays fixed in a laboratory set of coordinates. A more common point of view is to use molecular-orbital wave functions which are quantized in a frame rotating with the internuclear line. In such a frame, a wave function fixed in the laboratory frame would exhibit a continual rotational coupling between the σ_g and π_g molecular orbitals.

Consider the development of the wave function during a collision in which the distance of closest approach is smaller than R_c. Before the first crossing, the time-dependent molecular wave function for the $He^+ + He$ system is

$$\psi(t) = \psi_1 \exp\left(-\frac{i}{\hbar}\int_{-\infty}^{t} E_1(t')\,dt'\right).$$

At the first crossing, the wave function divides into two parts, namely, the incident wave function ψ_1 and the excited-state wave function ψ_2. In the approximation that the magnitude of the complex Landau-Zener transition probability p is small compared to unity (owing to the two-electron nature of the excitation process), the wave function immediately after the crossing is

$$\psi(t) \approx \psi_1 \exp\left(-\frac{i}{\hbar}\int_{-\infty}^{t} E_1(t')\,dt'\right) + p\psi_2^{(i)} \exp\left(-\frac{i}{\hbar}\int_{-\infty}^{t_i} E_1(t')\,dt' - \frac{i}{\hbar}\int_{t_i}^{t} E_2(t')\,dt'\right),$$

where terms of order $|p|^2$ in the coefficients of ψ_1 and $\psi_2^{(i)}$ have been neglected, and where subscript 1 denotes the initial $1s\sigma_g(2p\sigma_u)^2$ level, subscript 2 denotes the $(1s\sigma_g)^2 4d\sigma_g$ excited level, and superscripts indicate that the $4d\sigma$ state is evaluated with the symmetry axis along the internuclear line at the in (i) or out (o) position. As the crossing is traversed on the outer passage, the wave function divides again. Neglecting terms of order $|p|^2$, we have for the final wave function

$$\psi_f(t) \approx \left[p\psi_2^{(i)} \exp\left(-\frac{i}{\hbar}\int_{-\infty}^{t_i} E_1(t')\,dt' - \frac{i}{\hbar}\int_{t_i}^{t} E_2(t')\,dt'\right) + p^*\psi_2^{(o)} \exp\left(-\frac{i}{\hbar}\int_{-\infty}^{t_o} E_1(t')\,dt' - \frac{i}{\hbar}\int_{t_o}^{t} E_2(t')\,dt'\right)\right] + B\psi_1 \exp\left(-\frac{i}{\hbar}\int_{-\infty}^{t} E_1(t')\,dt'\right), \tag{18}$$

where B is the amplitude of the initial state at $t \to \infty$.

A transformation of the $4d\sigma$ functions to a frame with z axis along the incident-beam direction, taking into account that the $4d\sigma_g$ and $4d\pi_g$ states correlate with the $3p(m_l = 0)$ and $3p(m_l = \pm 1)$ atomic orbitals, respectively, gives the amplitudes a_0 and a_1 when the final level is in the $m_l = 0$ and

$m_l = \pm 1$ magnetic substates. The transformation is effected with the aid of rotation matrices $D_{uv}(n, n', n'')$, where n, n', and n'' are the Euler angles of the rotation. Aside from an overall phase factor, we find

$$a_0 = \langle \psi_f | 4d\sigma_g \rangle = |p| 2^{-1/2} (3\cos^2\alpha - 1)\cos A,$$
$$a_1 = \langle \psi_f | 4d\pi_g \rangle = i|p| 3^{1/2} (\sin\alpha\cos\alpha)\sin A, \tag{19}$$

where

$$A = \int_0^t \frac{[E_2(t') - E_1(t')]dt'}{\hbar} + \chi, \tag{20}$$

and χ is the phase of the Landau-Zener transition amplitude p.

From Eq. (19) it is clear that $\Delta\phi$ is a constant function of impact parameter and incident energy, and equals 90°. Variations around 90° are expected if other mechanisms contribute to the excitation. Also, the model predicts the phase difference to be constant independent of any assumed relation between the impact parameter and the scattering angle, and, in particular, independent of the value of R_c. In contrast, $|a_0|^2$ and $|a_1|^2$ are sensitive to all these parameters. A detailed comparison of the model with the present data has not been made, since the requisite potential energy curves are not available. Also, there is some doubt whether a simple relation between the scattering angle θ and impact parameter b can be found. If R_c is about 1 a.u., then one expects diffraction maxima and minima in the differential cross section if $a_0(b)$ cuts off sharply at R_c. The maxima and minima should be separated by an angle about equal to 0.09°, which is comparable to the angular resolution of the experiment. Thus a detailed calculation incorporating a partial wave analysis of the scattering may be required to fully compare theory and experiment.

---

*Work supported by the National Science Foundation.

[1]W. de Rijk, F. J. Eriksen, and D. H. Jaecks, Bull. Am. Phys. Soc. 19, 1230 (1974).
[2]G. Vassilev, G. Rahmat, J. Slevin, and J. Baudon, Phys. Rev. Lett. 34, 447 (1975).
[3]D. H. Jaecks, F. J. Eriksen, W. de Rijk, and J. Macek, Phys. Rev. Lett. 35, 723 (1975).
[4]F. J. Eriksen and D. H. Jaecks, *Electronic and Atomic Collisions, Abstracts of the Papers of the Ninth International Conference on the Physics of Electronic and Atomic Collisions*, edited by J. S. Risley and R. Geballe (Univ. of Washington Press, Seattle, 1975), p. 1148.
[5]J. van den Bos, G. J. Winter, and F. J. de Heer, Physica (Utr.) 40, 357 (1968).
[6]M. van der Wiel, Ph.D. thesis (Univ. of Amsterdam, 1971) (unpublished); R. Avida and S. Gorni, Nucl. Instrum. Methods 52, 125 (1967).
[7]S. J. Young, J. S. Murray, and J. R. Sheridan, Phys. Rev. 178, 40 (1969); R. H. McKnight and D. H. Jaecks, Phys. Rev. A 4, 2281 (1971); P. J. Martin and D. H. Jaecks, Phys. Rev. A 8, 2429 (1973).
[8]J. Bakos and J. Sziget, Acta Phys. 21, 149 (1966).
[9]S. Nagy, S. Fernandez, and E. Pollack, Phys. Rev. A 3, 280 (1971).
[10]M. Barat, D. Dhuicq, R. Francois, R. McCarroll, R. Piacentini, and A. Salin, J. Phys. B 5, 1343 (1972).
[11]F. J. de Heer and J. van den Bos, Physica (Utr.) 31, 365 (1965); L. Wolterbeck Müller and F. J. de Heer, *ibid.* 48, 345 (1970); and F. J. de Heer, L. Wolterbeck Müller, and R. Geballe, *ibid.* 31, 1745 (1965).
[12]H. D. Young, *Statistical Treatment of Experimental Data* (McGraw-Hill, New York, 1962), pp. 108 and 111.
[13]J. Macek and D. H. Jaecks, Phys. Rev. A 4, 2288 (1971).
[14]J. N. Bardsley, Phys. Rev. A 3, 1317 (1971).
[15]D. R. Bates and R. H. G. Reid, *Advances in Atomic and Molecular Physics* (Academic, New York, 1968), Vol. 4, p. 13.
[16]M. Barat and W. Lichten, Phys. Rev. A 6, 211 (1972).